



Computational framework for a systematic investigation of anionic redox process in Li-rich compounds

Tygesen, Alexander Sougaard; Chang, Jinhyun; Vegge, Tejs; García Lastra, Juan Maria

Published in:
npj Computational Materials

Link to article, DOI:
[10.1038/s41524-020-0335-4](https://doi.org/10.1038/s41524-020-0335-4)

Publication date:
2020

Document Version
Publisher's PDF, also known as Version of record

[Link back to DTU Orbit](#)

Citation (APA):
Tygesen, A. S., Chang, J., Vegge, T., & García Lastra, J. M. (2020). Computational framework for a systematic investigation of anionic redox process in Li-rich compounds. *npj Computational Materials*, 6(1), Article 65. <https://doi.org/10.1038/s41524-020-0335-4>

General rights

Copyright and moral rights for the publications made accessible in the public portal are retained by the authors and/or other copyright owners and it is a condition of accessing publications that users recognise and abide by the legal requirements associated with these rights.

- Users may download and print one copy of any publication from the public portal for the purpose of private study or research.
- You may not further distribute the material or use it for any profit-making activity or commercial gain
- You may freely distribute the URL identifying the publication in the public portal

If you believe that this document breaches copyright please contact us providing details, and we will remove access to the work immediately and investigate your claim.

ARTICLE OPEN



Computational framework for a systematic investigation of anionic redox process in Li-rich compounds

Alexander Sougaard Tygesen¹, Jin Hyun Chang¹✉, Tejs Vegge¹ and Juan Maria García-Lastra¹✉

Anionic redox processes play a key role in determining the accessible capacity and cycle life of Li-rich cathode materials for batteries. We present a framework for investigating the anionic redox processes based on data readily available from standard DFT calculations. Our recipe includes a method of classifying different anionic species, counting the number of species present in the structure and a preconditioning scheme to promote anionic redox. The method is applied to a set of Li_xMnO_3 ($1 \leq x \leq 2$) structures, with cationic disorder, to identify the evolution of anionic redox processes during cycling. Additionally, we investigate how different choices of exchange-correlation functionals affect the formation of anionic redox species. The preconditioning of the structures is shown to promote the formation of peroxo-like species. Furthermore, the choice of exchange-correlation functional has a large impact on the type of anionic redox species present, and thus care must be taken when considering localization in anionic species.

npj Computational Materials (2020)6:65; <https://doi.org/10.1038/s41524-020-0335-4>

INTRODUCTION

Anionic redox processes are currently an intensely studied topic in battery research as it allows a significant increase in the accessible energy capacity in Li-rich cathodes in lithium-ion batteries^{1,2}. Li_2MnO_3 is one of the Li-rich cathode materials where the anionic redox is known to make a dominant contribution to its high theoretical capacity of around 460 mAh g^{-1} ^{3–5}. Li_2MnO_3 has a layered rocksalt-type structure, and was initially thought to be chemically inert as Mn^{4+} in octahedral oxygen coordination cannot be oxidized to Mn^{5+} ⁶. However, it was found through electrochemical measurements that cycling was indeed possible^{7,8}. Many possible explanations for the cyclability were suggested, and anionic redox is regarded as one of the main contributors^{5,9}. Li_2MnO_3 suffers from a fast capacity fading, particularly in the initial cycling step¹⁰. Its fast capacity fading is also attributed to the anionic redox process, which leads to an irreversible and potentially dangerous evolution of oxygen gas^{7,10}.

It is desirable to promote reversible anionic redox processes while suppressing the irreversible ones, thereby achieving the maximum energy capacity without suffering from a poor cyclability. Optimizing the reversibility requires an in-depth understanding of the anionic redox processes, such as the correlation between the local environment of the oxygen species to its redox activity^{11,12}. A detailed understanding of the correlation can ultimately guide the design process of the new battery electrode materials and set desired operating conditions (e.g., operating temperature and voltage range) for the longevity of the batteries.

Computational methods such as density functional theory (DFT) allow one to probe the local processes on the atomic level, which are difficult to achieve using experimental techniques. In particular, DFT simulations allow one to carry out “controlled experiments” where specific atomic arrangements are imposed, and the corresponding electronic structures in the vicinity of individual atoms are analyzed. In the context of electronic structures, anionic redox is the presence of electron holes on the oxygen species, which leads to the change in its oxidation state^{5,13–18}.

Despite such detailed control, standard recipes and workflows for systematic investigations of anionic redox reactions in theoretical calculations are still lacking. Large-scale studies involving many calculations are becoming more popular, and these standard recipes/workflows are needed to carry out such studies efficiently. In computational research for battery electrode materials, the most prominent examples are (1) screening of materials for materials discovery using automated workflows^{19–22}, and (2) analysis of disordered materials^{9,23–26} using the cluster expansion method^{27–29}.

Two key aspects need to be carefully considered when studying anionic redox using DFT: a systematic method for classifying the type of anionic species and the choice of exchange-correlation functional. Anionic redox can manifest in several types of species, as a single oxygen ion, O^- , as short-bond oxygen pairs or as delocalized states in the O-2p bands. Short-bond oxygen pairs can emerge as peroxide, superoxide, and molecular oxygen, which we label collectively as peroxo-like species¹⁷. The fully lithiated structure of Li_2MnO_3 is shown in Fig. 1a, and a partially delithiated structure containing peroxo-like species is shown in Fig. 1b. We propose an algorithm for determining the types of anionic species present in the structures based on data readily accessible from standard DFT calculations.

The choice of exchange-correlation functional plays an important role as the self-interaction error in DFT makes the localization of electron holes challenging. Recent anionic redox reaction studies^{9,11,30} have employed the Heyd–Scuseria–Ernzerhof (HSE06)³¹ hybrid functional to avoid introducing a bias between the cationic and anionic redox reactions. Although the HSE06 functional allows one to describe the localized states⁹, it is accompanied by a high computational cost, which makes it unsuitable for larger-scale studies. Furthermore, HSE is a highly tunable functional with a parameter α , and it has been shown that tuning α leads to different results that do not consistently outperform the alternatives with lower computational costs^{32–34}.

A common approach when studying transition metal (TM) oxides is to use the generalized gradient approximation (GGA) functionals such as the Perdew–Burke–Ernzerhof (PBE)³⁵ functional and apply a

¹Department of Energy Conversion and Storage, Technical University of Denmark, DK-2800 Kgs. Lyngby, Denmark. ✉email: jchang@dtu.dk; jmgl@dtu.dk

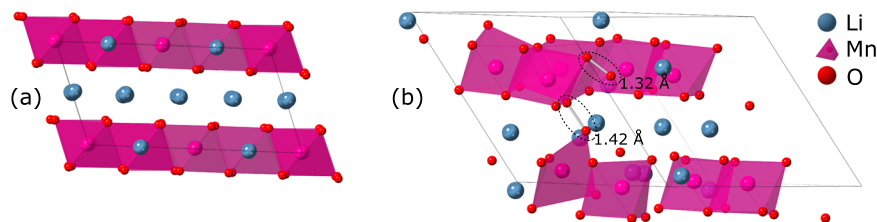


Fig. 1 Structure of Li_xMnO_3 . Structure of layered rocksalt-type Li_xMnO_3 , which in general is considered as a rocksalt lattice with a disordered cationic sublattice. **a** Fully lithiated Li_2MnO_3 . **b** Partially lithiated $\text{Li}_{1.22}\text{MnO}_3$ containing both superoxide and peroxide, highlighted by a dashed black circle. The bond with 1.32 Å is identified as superoxide, and the bond with 1.42 Å as a peroxide. The sum of local magnetic moments on the superoxide and peroxide were $0.83\mu_B$ and $0.11\mu_B$, respectively.

Hubbard U correction on the TM- d orbitals. However, this approach is problematic for systems where both cationic and anionic localization may occur since the former will be favored over the latter. One could also apply the + U correction on the O- p orbitals, which introduces an additional parameter to balance. Although not as common as + U corrections on TM 3d orbitals, the + U corrections on O- p orbitals have been applied for the study of oxides^{36–38}, peroxides^{37,39}, and superoxides^{37,40} when electrons are found to be strongly localized on these orbitals. The strongly constrained and appropriately normed (SCAN)⁴¹ functional from the meta-GGA family is a less expensive alternative compared to the hybrid functionals. It has recently been gaining popularity as this non-empirical and parameter-free functional has been shown to provide an improved description of the band gaps and localized states compared to those of the GGA functionals^{42–44}. In this work, we compare the evolution of anionic redox processes during delithiation for the PBE+ U approach to the SCAN functional as these are the two most viable candidates for large volumes of calculations. Furthermore, we perform HSE06 calculations as a reference for the computationally cheaper methods since the size of the dataset still allows for hybrid calculations.

Another crucial issue is that the structural optimization algorithm may be “trapped” in a local energy minimum configuration. The formation of short distance oxygen bonds is often accompanied by a transition barrier⁹, preventing the classical relaxation schemes from locating such states. Here, we propose a preconditioning scheme based on the Ewald summation⁴⁵ energies in order to promote the formation of localized anionic redox and to investigate the stability of peroxo-like species in the lattice.

Chen and co-workers⁴⁶ applied a cluster expansion method to Li_2MnO_3 in order to determine the most stable structure during cycling and to reproduce information such as charge/discharge voltage curves. Cluster expansion approaches may require a large number of DFT calculations, and Chen et al. assumed the structure remained layered, which reduces the considered configuration space. While Li_2MnO_3 is known to be a layered structure at full lithiation, it is also known to undergo phase transitions^{7,10,47,48}, and similar Li-rich structures are known to become disordered during delithiation⁴⁹. In this work, we lift the constraint where the material remains layered and consider the structures in the rocksalt lattice where the Mn and Li species share the cationic sublattice (i.e., full cationic disorder where each cationic site can be occupied by either Mn, Li or Li vacancy, as other authors have done for similar systems²⁵); the evolution of anionic redox processes is analyzed on cation-disordered structures, which lays the ground for future cluster expansion studies.

RESULTS

A set of 101 structures with varying degree of substitutional disorder and lithiation levels are generated for this study. The unaltered initial configurations where all of the atoms are placed at the ideal lattice sites are denoted as “pristine” structures. An

Ewald preconditioning has been applied to all of the configurations to promote the electronic localization, which has led to an additional 85 initial structures that are denoted as “Ewald” structures. Ewald structures are constructed by promoting the creation of peroxo-like species around those crystal sites where the Coulombic potential is the lowest. A detailed information on the generation of the initial structures and Ewald preconditioning can be found in the Methods section. Both pristine and Ewald structures are calculated while the atomic positions and the cell geometry are optimized.

Furthermore, four functionals were applied to the entire dataset: the SCAN functional; PBE with a Hubbard U correction on the Mn- d orbitals, denoted as PBE+ U_{Mn} ; PBE with + U on Mn- d and O- p orbitals, denoted as PBE+ $U_{Mn,O}$; and HSE06 adjusted to $\alpha = 0.17$ in order to match the band gap of Li_2MnO_3 to that of G_0W_0 ¹¹. As a sanity check, we confirmed that all four functionals correctly predict the fully layered and ordered structure to be the most stable one, as reported in the literature²⁶.

Classification of redox activity

An algorithm for determining the types of local anionic species present in the structures is developed, and the flowchart describing the algorithm is illustrated in Fig. 2. The presented algorithm avoids manual inspection of individual data points, making the analysis more robust and reproducible. The algorithm categorizes the localized anionic species into singular oxygen (O^-), O_2^{3-} species, peroxide (O_2^{2-}), superoxide (O_2^-) and molecular oxygen (O_2), which, respectively, have 1, 1, 2, 3, and 4 localized holes. The oxygen species without any localized hole is labelled as “lattice oxygen”. The anionic species are categorized mainly based on the bond distance between two oxygen atoms, d_{OO} , and the local magnetic moment, μ . The hole localization in the oxygen pair reduces the bond length due to the removal of electrons in antibonding orbitals, and the resulting spin-pairing can be observed via local magnetic moments of the oxygen pairs. The peroxide and superoxide shown in Fig. 1b are identified using the scheme from Fig. 2.

It is more difficult to identify a hole localized on a single oxygen (O^-) due to the lack of significant structural distortions around it. We here chose to use the Bader charge to identify the presence of O^- species, as opposed to the local magnetic moments, as contributions to the magnetic moments from delocalized holes can be difficult to distinguish from that of localized holes (an example of this is depicted in supplementary Fig. 8). More specifically, we use the deviation of the Bader charge in the oxygen species from the average of every oxygen species in structures at the same lithiation level and denote it as Δq_{O} ($\Delta q_{\text{O}} = q_{\text{O}} - \langle q_{\text{O}} \rangle$, where $\langle q_{\text{O}} \rangle$ is the average Bader charge of all oxygen species at a given lithiation level). The threshold of Δq_{O} for distinguishing O^- from the lattice oxygen is set to $-0.45 e^-$ based on observation (see supplementary information for more details). It is noted that the cutoff values in Fig. 2 are determined

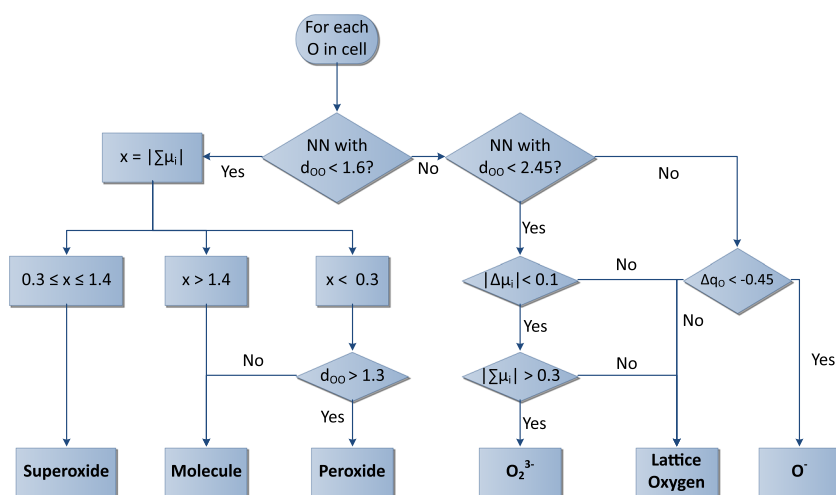


Fig. 2 Flowchart of classification algorithm. Flowchart of the algorithm for classifying the anionic species. Nearest oxygen neighbor and the local magnetic moment are denoted as NN and μ_i , respectively. $\sum\mu_i$ is the sum of the local magnetic moments on the considered oxygen pair, $\Delta\mu_i$ is the difference between the magnetic moments of two species, and d_{OO} is the distance between the nearest oxygen pairs in Å. The change in Bader charge is denoted as Δq_O .

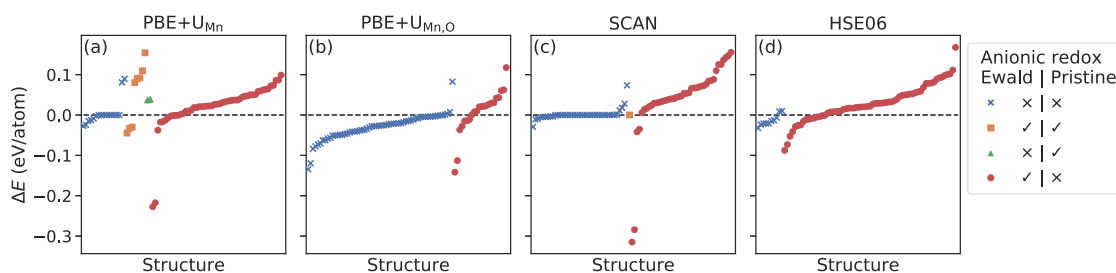


Fig. 3 Ewald preconditioning stability. Relative energies of the structures relaxed from the Ewald-preconditioned and pristine structures for the considered functionals. Labels indicate the presence of the peroxo-like species after the relaxation. The black dashed line represents $\Delta E = 0$. Structures are sorted by category and by energy.

heuristically, which can serve as a guide value for further studies beyond Li_2MnO_3 .

Cationic redox activity is another crucial aspect to consider as it is the main contributor of the redox activity for most cathode materials. While magnetic moments have been used previously to identify TM redox activity^{9,30}, identifying the oxidation state of Mn from the magnetic moment is challenging, especially when vacancies are introduced upon delithiation. Li vacancies distort the TM–O octahedra, and the crystal field splitting in an octahedral field is no longer applicable. We opted to use the change in Bader charge for distinguishing Mn species ($\Delta q_{\text{Mn}} = q_{\text{Mn}} - \langle q_{\text{Mn}} \rangle$, where $\langle q_{\text{Mn}} \rangle$ is the average Bader charge of all Mn species at a given lithiation level). A cutoff of $0.1 e^-$ was chosen, i.e., $\Delta q_{\text{Mn}} > 0.1$ means that Mn^{4+} has been reduced to Mn^{3+} . We have compared Δq_{Mn} in Mn_2O_3 and MnO_2 , which, respectively, have the nominal oxidation state +3 and +4. Δq_{Mn} is computed to be $0.10 e^-$, $0.05 e^-$, and $0.11 e^-$ for $\text{PBE}+U_{\text{Mn}}$, $\text{PBE}+U_{\text{Mn},\text{O}}$, and SCAN, respectively, which suggests that $0.1 e^-$ is a suitable choice. It may seem surprising that a $\Delta q_{\text{Mn}} = 0.10 e^-$ corresponds to a +1 change in the oxidation state. This is due to the charge self-regulation in TM complexes where the TM atoms tend to maintain a constant local charge under external perturbations⁵⁰.

The possibility of Mn to oxidize is not considered in this study, although it has recently been claimed that Mn can be found in +7 oxidation state⁵¹. We carefully checked that none of the Mn ions in any of the structures studied had any +7 oxidation state. It may seem counter-intuitive to consider the reduction of Mn (Mn^{4+} to Mn^{3+}) upon delithiation while not considering the oxidation. The oxidation would require Mn^{4+} to oxidize to Mn^{6+} or Mn^{7+}

because the Mn^{5+} state is highly unlikely to occur⁵². Cationic reduction, on the other hand, has been observed in other materials where anionic redox processes take place. One noted example is Li_3VS_4 where V^{5+} reduces to V^{4+} during delithiation concomitantly to anionic local reduction of S^{2-} to $(\text{S}_2)^{2-53}$.

Preconditioning and the formation of peroxo-like species

The Ewald preconditioning scheme was applied to the entire set of 101 structures in order to promote the formation of peroxo-like species by manually overcoming the transition barriers. The relative energies of the structures relaxed from the Ewald-preconditioned structures with respect to the structures relaxed from the pristine structures are shown in Fig. 3. Here, the relaxed structures are classified into four categories based on the presence of the peroxo-like species: absence of peroxo-like species in both pristine and the Ewald-preconditioned structures (blue cross); presence of peroxo-like species in both cases (orange square); peroxo-like species present only in the pristine structures (green triangle); peroxo-like species present only in the Ewald-preconditioned structures (red circle). The relative energy, ΔE , is defined as $\Delta E = E_{\text{Ewald}} - E_{\text{pristine}}$, where E is the total DFT energy. A negative ΔE means that the energy of the structure relaxed from the Ewald structure is more stable, and vice versa. It should be noted that DFT has a systematic error, which overestimates the stability of peroxo-like species⁵⁴. However, this systematic error does not affect the results of this study (see supplementary information for more details).

It can be seen in Fig. 3 that the Ewald preconditioning promotes the anionic redox activity. A significant portion of the dataset corresponds to the case where the peroxo-like species are present only in the Ewald-preconditioned structures (red circle)—75%, 27%, 51%, and 87% for PBE+U_{Mn}, PBE+U_{Mn,O}, SCAN, and HSE06 functionals, respectively. On the other hand, there are only two instances where the opposite is true (green triangle). These observations support our original motivation where the energy barrier may prevent the classical relaxation scheme from locating the localized holes.

Interestingly, a majority of the red circles are above $\Delta E = 0$, indicating that the anionic redox does not always stabilize the system. In other words, the presence of anionic redox does not necessarily result in more stable configurations. The Ewald preconditioning causes formation of the peroxo-like species even when it is not energetically favorable. However, preconditioning has a benefit of breaking the initial symmetries present in the pristine structures. Two red circles with large negative ΔE values in all of the three functionals are good examples showcasing the benefit of breaking the initial symmetry that the pristine structures were not able to escape.

While preconditioning promotes the formation of peroxo-like species, it does not guarantee the formation. Surprisingly, there are also rare cases where the peroxo-like species are found only in the pristine structures (two green triangles). In addition, a substantial portion of the structures in Fig. 3 shows no formation of peroxo-like species (blue crosses) for all three functionals considered. Furthermore, many of the structures in Fig. 3a, c have $\Delta E = 0$, indicating that the pristine and Ewald-preconditioned structures converged to nearly identical final structures. Converging to nearly identical structures is more pronounced for the SCAN functional when no peroxo-like species are observed. Most of the blue crosses for PBE+U_{Mn,O} functional in Fig. 3b, on the other hand, lie below $\Delta E = 0$, which further highlights the importance of escaping local minima even in the absence of anionic redox activity.

Preconditioning promotes the formation of peroxo-like species, which aligns with the initial expectations. However, peroxo-like species are often energetically less favorable, and preconditioning does not necessarily result in the more stable configurations. It is difficult to escape the local energy minimum configurations for both the pristine and Ewald-preconditioned structures. Therefore, one should be cautious in drawing conclusions on the formation of anionic redox species based on either one method; it is important to start the calculations with more than one initial structure and select the most stable configuration for the analysis.

Evolution of anionic redox

The evolution of oxygen gas during cycling of Li₂MnO₃ has been attributed to the formation of peroxo-like species and O⁻, which eventually form peroxo-like species⁹. The evolution of the localized anionic redox species at varying lithiation levels are investigated by counting the average number of holes in each anionic redox species at each lithiation level as shown in Fig. 4. Assuming no cationic reduction occurs during delithiation, every available hole would be supplied from the removal of Li; the number of holes would thus match the number of Li removed. However, the total amount of holes in the system is slightly higher than the number of removed Li in some cases, owing to the reduction of Mn⁴⁺ to Mn³⁺ releasing additional holes. As the amount of electrons in the system must be conserved, holes which have not been localized in O are considered delocalized in the O-2p bands for the purposes of this study.

A clear trend where the number of localized holes (thus the number of anionic redox species) increases as Li₂MnO₃ is further delithiated, can be seen in Fig. 4. The observed trend aligns well with an increased number of Li vacancies leading to an increase in

the number of holes, which in turn increases the probability in which the holes get localized to form the anionic redox species. As the formation of these species are the main driving force for the formation of oxygen gas, evolution of oxygen gas is expected to be more profound at higher delithiation levels¹³. Previous calculations on Li₂MnO₃ have shown that a substantial delithiation was required for the formation of peroxides under the restriction where the structures remain layered³⁰. However, we observed the possibility of peroxide formation at very early stages of delithiation when layering restriction is lifted.

The +U correction counteracts the self-interaction errors in DFT and promotes the localization onto specific atomic orbitals. It can be seen from Fig. 4c, d that applying +U on the O-*p* orbitals results in a higher likelihood of forming O⁻ species rather than peroxo-like species compared to the other two functionals; PBE+U_{Mn,O} stabilizes the O⁻ localization more than the peroxo-like localization by a factor of two. The prevalence of the O⁻ formation can also be seen in Fig. 3b, where the number of structures without peroxo-like species (blue crosses) is larger compared to the other functionals. Furthermore, PBE+U_{Mn,O} promotes the largest amount of reduction in the Mn, moving additional holes from the Mn ions onto the oxygen species.

PBE+U_{Mn} and HSE functionals show the most pronounced hole localization on oxygen dimers upon delithiation. However, while in the former the holes are evenly distributed among different species, the latter shows a clear preference for hole localization in peroxide ions and single O⁻ species. The preference for peroxide ions in HSE when compared to PBE+U_{Mn} was expected since it has been reported that the relative formation energies of alkali peroxides versus alkali superoxides (i.e., $\Delta H^{\text{form}}(\text{MO}_2) - \Delta H^{\text{form}}(\text{M}_2\text{O}_2)$) is ~0.4 eV larger in HSE than in PBE+U_{Mn}³⁷. It was also expected that the amount of single O⁻ species was larger in HSE than in PBE+U_{Mn} since the former corrects the SIE in O-2*p* orbital while the latter does not.

So far, we have discussed the evolution of the anionic redox averaging the results of all the structures at each lithiation level with equal weight (results in the panels denoted as $T \rightarrow \infty$ in Fig. 4). Figure 4 also shows a thermodynamic averaging at each lithiation level including the Boltzmann factor of the relative energies (results in the panels denoted as $T = 300$ K in Fig. 4), calculated with the same procedure detailed by Loftager et al.⁵⁵. We observe that the main features of the equally averaged results are maintained with the Boltzmann weighted average, barring the SCAN functional, where most of the signal from the peroxo-like species disappears. This underlines that the peroxo-like species are relatively unstable within the SCAN functional.

Structural stability versus oxygen release

The stability of Li₂MnO₃ has been extensively discussed in the literature^{56–59}. Although the purpose of this study is not to find the minimum energy structure for each lithiation level, we have analyzed the structural stability for the lowest energy structure at each lithiation level, which contains at least one oxygen dimer. This has been done according to

$$\text{Stability} = E(\text{O}_2) + E(\text{Li}_{xy}\text{Mn}_y\text{O}_{3y-2}) - E(\text{Li}_{xy}\text{Mn}_y\text{O}_{3y}) \quad (1)$$

where $E(\text{O}_2)$ is the energy of oxygen molecule in gas phase, $E(\text{Li}_{xy}\text{Mn}_y\text{O}_{3y})$ is the energy of the lowest energy structure with at least one oxygen dimer and $E(\text{Li}_{xy}\text{Mn}_y\text{O}_{3y-2})$ is the energy of the same structure where one oxygen dimer is removed (we relaxed the structure after we removed a dimer). The stability of the most stable structure at all lithiation levels are shown in Fig. 5. It should be noted that the molecular oxygen corrected due to the error cancellation (the error in the energy of the oxygen dimer species within the lattice is similar to the error in molecular oxygen)³⁷.

The stability versus oxygen evolution seems to be strongly dependent on the choice of functional. None of the lowest energy

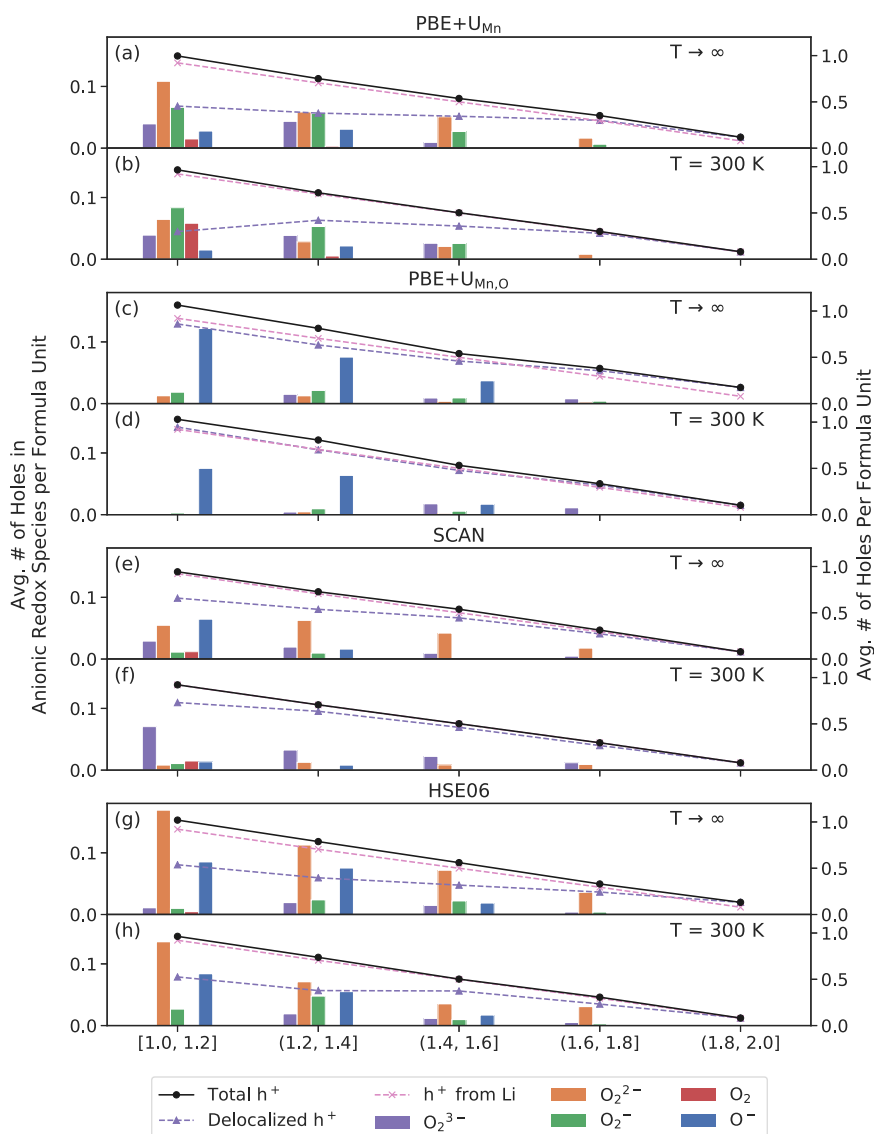


Fig. 4 Evolution of anionic redox. Average number of anionic redox species at varying levels of lithiation. Lines belong to the secondary y-axis, and denote the average delocalized and total amount of holes in the cell per formula unit, as well as the amount of holes provided by removal of Li. $T = 300$ K represents the Boltzmann averaged concentrations at $T = 300$ K while $T \rightarrow \infty$ represents the non-weighted average concentrations.

structures are stable against oxygen evolution for SCAN functional, which can be deduced when comparing Fig. 4e, f; the signal from peroxides vanishes for the average Boltzmann distribution when $T = 300$ K. Around two thirds of the structures are stable for PBE + $U_{Mn,O}$ and HSE06, while around one-third of the structures are stable for PBE + U_{Mn} . The functionals that better promote the localization also lead to a higher stability.

Local ordering

It is important to also consider the local structuring around these species containing the localized anionic redox in order to identify which local environments promote the formation of peroxo-like species⁶⁰. In Fig. 6 the distance from the center of mass (COM) of the anionic redox species to the nearest metal species is shown. In Fig. 6a, we find that the more oxidized the peroxo-like species the larger the distance they are from the nearest Mn ion, which is as expected from the electrostatic point of view. It is worth noting that the oxygen dimers maintain their chemical bond with the nearest Mn ion (the average distance between Mn and

O_2^{3-} , peroxides and superoxides is ~ 2.1 , ~ 2.1 , and ~ 2.3 Å, respectively), with an exception of the molecular oxygen. This resembles the experimentally observed bonds between transition metals and oxygen dimer species in transition metal peroxo/oxide compounds⁶¹. In contrast, the localized O^- are no longer bonded to Mn ions (average Mn–O distance larger than 3 Å) with few exceptions where their distance to Mn ions is ~ 1.8 Å using the HSE06 functional. On the other hand, the oxidation states of the dimer species hardly has any influence on the Li–O distances as shown in Fig. 6b.

DISCUSSION

A framework for investigating the anionic redox processes using DFT calculations has been developed. The presented method is capable of estimating the amount of localized anionic redox and the trends in the evolution of anionic redox during cycling, all based on data readily available from standard DFT calculations. Our method serves as a recipe for other computational studies for understanding and designing of stable Li-rich materials. The

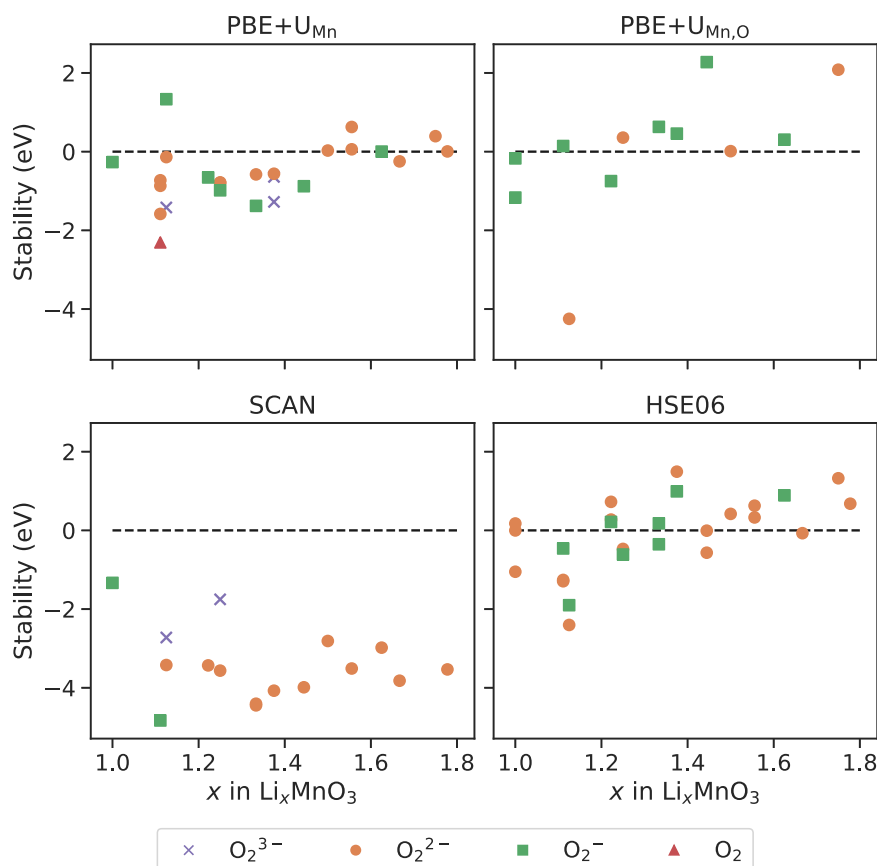


Fig. 5 Stability versus oxygen release. Stability versus oxygen release for most stable structure, which contains at least one peroxo-like species at each lithiation level. Points above the dashed line indicate that the structure is stable versus oxygen release while the opposite is true for the points below the dashed line.

recipe allows one to classify, and subsequently quantify, the types of anionic redox species in a given set of structures, which in turn allows for further investigations for stabilizing and controlling the anionic redox processes in the material design.

A preconditioning scheme was applied to the initial set of pristine structures in order to promote the formation of peroxo-like species. The preconditioning resulted in an increased number of peroxo-like species, but their presence was not always energetically favorable. The dependence on the initial structure highlights the fact that the structure optimizer used in DFT calculations finds a local energy minimum structure, and care must be given in analyzing the presence of the anionic redox species.

The choice exchange-correlation functional was shown to have a significant impact on the amount of anionic redox during the delithiation process. While each functional resulted in different tendencies in how anionic redox presents itself, it is difficult to judge the performance of the functionals without experimental references of this kind. However, as a sanity check, the most stable structure at full lithiation was found to agree with the experimentally observed ordered layered Li_2MnO_3 , as shown in Fig. 1a. The SCAN and $\text{PBE}+U_{\text{Mn}}$ functionals both find comparable amounts of peroxide species; however, they disagree on the amount of superoxide. Conversely, the $\text{PBE}+U_{\text{Mn},\text{O}}$ functional prefers the formation of O^- over peroxo-like species.

We found that the formation of localized anionic species begins early in the delithiation phases. As this was not observed in previous DFT studies, the assumption of perfect layering was restricting the peroxo formation, as well as the structural initialization. Furthermore, the structure needs to be considered in a disordered form for any cluster expansion model or large-

scale screening studies on these types of material in order to describe the structural transformations during delithiation. A careful consideration of the functional choice was also seen to be crucial, as this has a large influence on the general trends in the structure database.

METHODS

Preparation of preconditioned structures using Ewald summation

In order to assist the structure optimization algorithm in the formation of peroxo-like species, we manually compress an oxygen pair. However, due to the size of the configurational space, it is not feasible to initialize the system with every possible oxygen pair compression. Instead, we developed a scheme based on the Ewald summation^{45,62,63} technique in order to locate the most probable locations for the peroxo-like species formation.

We assume the two most probable peroxo-like species to form are peroxides and superoxides. A peroxide species requires the localization of 2 holes (h^+), and a superoxide requires 3 h^+ . Each Li vacancy in the cell provides a single h^+ . Under the constraint of charge neutrality, there are only a certain number of ways to place any number of peroxides and superoxides in the cell, depending on the number of vacancies. The oxygen pairs with the lowest Ewald summation energies are then selected as the most likely candidates for peroxo-like species formation. The Ewald summation was calculated using the pymatgen⁶⁴ code, and the Ewald preconditioning scheme is summarized as follows:

- (1) Count number of h^+ and determine all possible permutations of superoxide and peroxide species which fulfill the charge neutrality.
- (2) Initialize nominal oxidation states +1 for Li, +4 for Mn, and -2 for O.
- (3) Distribute remaining charge from the Li vacancies evenly across all atoms in the cell such that the total oxidation state is 0.
- (4) Calculate site energies from the Ewald summation.

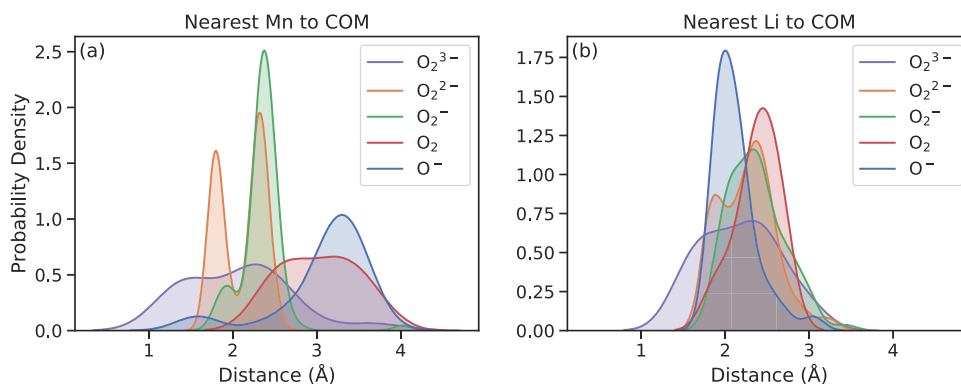


Fig. 6 Local distance distributions. Probability distributions of the distance of the anionic redox species COM to the nearest metal species. The distributions were fitted using a kernel density estimate. **a** Distance to the nearest Li. **b** Distance to the nearest Mn.

- (5) Locate oxygen pairs with the lowest average site energy.
- (6) Place 1 peroxo-like species, prioritizing the placement of superoxides first.
 - Peroxide: set bond length to 1.53 Å and oxidation state of each oxygen in the pair to -1 .
 - Superoxide: set bond length to 1.30 Å and oxidation state of each oxygen in the pair to -0.5 .
- (7) Distribute remaining negative charge over all other atoms such that the total oxidation state is 0.
- (8) Repeat step 4 until all possible peroxo-like species have been placed.
- (9) Repeat step 1 for all possible permutations in new structures.

Preparation of structures

The structures were prepared in the Atomic Simulation Environment (ASE)⁶⁵. Disordered Li-rich Li_2MnO_3 has a rocksalt lattice with Li and Mn sharing the cationic sites and O occupying the anionic sites. In order to properly sample different configurations, supercells of varying sizes were used, with the largest being $3 \times 3 \times 3$. Additionally, Li vacancies are introduced into the cell, which further increases the configurational space. However, as Li_xMnO_3 is known to release oxygen during cycling, we limit our study to $1 \leq x \leq 2$ to capture the behavior of the initial cycle. As it is practically not feasible to sample every configuration, an initial population of 35 structures were generated randomly, and 66 subsequent structures were generated using simulated annealing technique to find the minimum energy configurations from a cluster expansion fit using the CLEASE⁶⁶ software package. A total of 101 disordered configurations were generated at varying degrees of lithiation. Application of the Ewald preconditioning scheme resulted in an additional 85 structures.

Computational details

The calculations were performed in the Vienna ab initio Simulation Package (VASP) DFT code^{67,68} with a plane wave basis set, using a 650 eV cutoff for the valence electrons. The core electrons were treated in the projector augmented wave (PAW)⁶⁹ formalism. The k -space was sampled using a Γ -centered Monkhorst-Pack grid⁷⁰ with a k -point density of 3.5 points per Å⁻¹. Default VASP magnetic moments were used, and therefore only ferromagnetic orderings were considered. The atomic positions and cell were relaxed until the force per atom is converged to 0.05 eV Å⁻¹ or less using the conjugate gradient algorithm as implemented in VASP, and the total energy is converged to within 10^{-5} eV.

We employed four different functionals: the meta-GGA functional, SCAN⁴¹; the GGA+U approach⁷¹ with the PBE³⁵ functional, with the correction of $U = 3.9$ eV placed on the Mn- d orbitals, as recommended by the materials project¹⁹; a PBE+U calculation with $U = 3.9$ eV on the Mn- d orbitals and $U = 6$ eV on the O- p orbitals, which has been previously used for the study of oxides^{36,38}, peroxides³⁹ and superoxides⁴⁰; and finally, the HSE06 functional with $\alpha = 0.17$, which reproduces the G_0W_0 band gap of Li_2MnO_3 ²⁶—in order to maintain a reasonable computational time, the k -point density was reduced to one-third for the HSE06 calculations. The

Hubbard- U corrections have been normalized, using a custom modification of the VASP code⁴⁰.

DATA AVAILABILITY

All the initial structures and the corresponding resulting relaxed structures presented in this work are available on DTU Data with the identifier “doi:10.11583/DTU.10264988”.

Received: 8 November 2019; Accepted: 27 April 2020;

Published online: 29 May 2020

REFERENCES

1. Grimaud, A., Hong, W. T., Shao-Horn, Y. & Tarascon, J. M. Anionic redox processes for electrochemical devices. *Nat. Mater.* **15**, 121–126 (2016).
2. Assat, G. & Tarascon, J. M. Fundamental understanding and practical challenges of anionic redox activity in Li-ion batteries. *Nat. Energy* **3**, 1–14 (2018).
3. Xiang, Y. & Wu, X. Enhanced electrochemical performances of Li_2MnO_3 cathode materials by Al doping. *Ionic* **24**, 83–89 (2018).
4. Xiong, L., Sun, M., Xu, Y., Du, X. & Xiao, X. Synthesis of carbon coated Li_2MnO_3 cathode material with enhanced rate capability for lithium-ion batteries. *Solid State Ionic* **325**, 170–175 (2018).
5. Zhao, C. et al. Review on anionic redox for high-capacity lithium- and sodium-ion batteries. *J. Phys. D Appl. Phys.* **50**, 183001 (2017).
6. Sathiyaraj, M. et al. High performance $Li_2Ru_{1-y}Mn_yO_3$ ($0.2 \leq y \leq 0.8$) cathode materials for rechargeable lithium-ion batteries: Their understanding. *Chem. Mater.* **25**, 1121–1131 (2013).
7. Robertson, A. D. & Bruce, P. G. Mechanism of electrochemical activity in Li_2MnO_3 . *Chem. Mater.* **15**, 1984–1992 (2003).
8. Yabuuchi, N., Yoshii, K., Myung, S. T., Nakai, I. & Komaba, S. Detailed studies of a high-capacity electrode material for rechargeable batteries, Li_2MnO_3 - $LiCo_{1/3}Ni_{1/3}Mn_{1/3}O_2$. *J. Am. Chem. Soc.* **133**, 4404–4419 (2011).
9. Chen, H. & Islam, M. S. Lithium extraction mechanism in Li-rich Li_2MnO_3 involving oxygen hole formation and dimerization. *Chem. Mater.* **28**, 6656–6663 (2016).
10. Rana, J. et al. Structural changes in Li_2MnO_3 cathode material for Li-ion batteries. *Adv. Energy Mater.* **4**, 1300998 (2014).
11. Seo, D. H. et al. The structural and chemical origin of the oxygen redox activity in layered and cation-disordered Li-excess cathode materials. *Nat. Chem.* **8**, 692–697 (2016).
12. Xie, Y., Saubanère, M. & Doublet, M.-L. Requirements for reversible extra-capacity in Li-rich layered oxides for Li-ion batteries. *Energy Environ. Sci.* **10**, 266–274 (2017).
13. Saubanère, M., McCalla, E., Tarascon, J. M. & Doublet, M. L. The intriguing question of anionic redox in high-energy density cathodes for Li-ion batteries. *Energy Environ. Sci.* **9**, 984–991 (2016).
14. Luo, K. et al. Charge-compensation in 3d-transition-metal-oxide intercalation cathodes through the generation of localized electron holes on oxygen. *Nat. Chem.* **8**, 684–691 (2016).
15. Muhammad, S. et al. Evidence of reversible oxygen participation in anomalously high capacity Li- and Mn-rich cathodes for Li-ion batteries. *Nano Energy* **21**, 172–184 (2016).

16. McCalla, E. et al. Visualization of O-O peroxo-like dimers in high-capacity layered oxides for Li-ion batteries. *Science* **350**, 1516–1521 (2015).
17. Sathiya, M. et al. Reversible anionic redox chemistry in high-capacity layered-oxide electrodes. *Nat. Mater.* **12**, 827–835 (2013).
18. Dong, X. et al. Towards low-cost, high energy density Li_2MnO_3 cathode materials. *J. Mater. Chem. A* **3**, 670–679 (2015).
19. Jain, A. et al. The Materials Project: a materials genome approach to accelerating materials innovation. *APL Materials* **1**, 011002 (2013).
20. Katcho, N. A. et al. An investigation of the structural properties of Li and Na fast ion conductors using high-throughput bond-valence calculations and machine learning. *J. Appl. Crystallogr.* **52**, 148–157 (2019).
21. Curtarolo, S. et al. AFLOW: an automatic framework for high-throughput materials discovery. *Comput. Mater. Sci.* **58**, 218–226 (2012).
22. Pizzi, G., Cepellotti, A., Sabatini, R., Marzari, N. & Kozinsky, B. AiIDA: automated interactive infrastructure and database for computational science. *Comput. Mater. Sci.* **111**, 218–230 (2016).
23. Persson, K., Hinuma, Y., Meng, Y. S., Van der Ven, A. & Ceder, G. Thermodynamic and kinetic properties of the Li-graphite system from first-principles calculations. *Phys. Rev. B* **82**, 125416 (2010).
24. Ji, H. et al. Computational investigation and experimental realization of disordered high-capacity Li-ion cathodes based on Ni redox. *Chem. Mater.* **31**, 2431–2442 (2019).
25. Das, H., Urban, A., Huang, W. & Ceder, G. First-principles simulation of the (Li-Ni-vacancy)O phase diagram and its relevance for the surface phases in Ni-rich Li-ion cathode materials. *Chem. Mater.* **29**, 7840–7851 (2017).
26. Seo, D. H., Urban, A. & Ceder, G. Calibrating transition-metal energy levels and oxygen bands in first-principles calculations: accurate prediction of redox potentials and charge transfer in lithium transition-metal oxides. *Phys. Rev. B Condens. Matter Mater. Phys.* **92**, 1–11 (2015).
27. Sanchez, J. M., Ducastelle, F. & Gratias, D. Generalized cluster description of multicomponent systems. *Phys. A Stat. Mech. Appl.* **128**, 334–350 (1984).
28. Fontaine, D. D. in *Solid State Physics* (eds. Ehrenreich, H., Turnbull, D.) Vol. 47, pp 33–176 (Academic Press, 1994).
29. Zunger, A. in *Statics and Dynamics of Alloy Phase Transformations* (eds. Turchi, P. E. A., Gonis, A.) pp 361–419 (Springer US, Boston, 1994).
30. Maruszczyk, A. et al. Oxygen activity and peroxide formation as charge compensation mechanisms in Li_2MnO_3 . *J. Mater. Chem. A* **5**, 15183–15190 (2017).
31. Krukau, A. V., Vydrov, O. A., Izmaylov, A. F. & Scuseria, G. E. Influence of the exchange screening parameter on the performance of screened hybrid functionals. *J. Chem. Phys.* **125**, 224106 (2006).
32. Tripkovic, V., Hansen, H. A., Garcia-Lastra, J. M. & Vegge, T. Comparative DFT+U and HSE study of the oxygen evolution electrocatalysis on perovskite oxides. *J. Phys. Chem. C* **122**, 1135–1147 (2018).
33. Kokott, S., Levchenko, S. V., Rinke, P. & Scheffler, M. First-principles supercell calculations of small polarons with proper account for long-range polarization effects. *N. J. Phys.* **20**, 033023 (2018).
34. Ong, S. P., Chevrier, V. L. & Ceder, G. Comparison of small polaron migration and phase separation in olivine LiMnPO_4 and LiFePO_4 using hybrid density functional theory. *Phys. Rev. B Condens. Matter Mater. Phys.* **83**, 75112 (2011).
35. Perdew, J. P., Burke, K. & Ernzerhof, M. Generalized gradient approximation made simple. *Phys. Rev. Lett.* **77**, 3865–3868 (1996).
36. Pardo, V. & Pickett, W. E. Magnetism from 2p states in alkaline earth monoxides: trends with varying N impurity concentration. *Phys. Rev. B* **78**, 134427 (2008).
37. Christensen, R., Hummelshøj, J. S., Hansen, H. A. & Vegge, T. Reducing systematic errors in oxide species with density functional theory calculations. *J. Phys. Chem. C* **119**, 17596–17601 (2015).
38. Nolan, M. & Watson, G. W. Hole localization in Al doped silica: a DFT+U description. *J. Chem. Phys.* **125**, 144701 (2006).
39. Garcia-Lastra, J. M., Myrdal, J. S., Christensen, R., Thygesen, K. S. & Vegge, T. DFT +U study of polaronic conduction in Li_2O_2 and Li_2CO_3 : implications for Li-air batteries. *J. Phys. Chem. C* **117**, 5568–5577 (2013).
40. Mathiesen, N. R., Yang, S., Garcia-Lastra, J. M., Vegge, T. & Siegel, D. J. Charge transport in alkali-metal superoxides: a systematic first-principles study. *Chem. Mater.* **31**, 9156–9167 (2019).
41. Sun, J., Ruzsinszky, A. & Perdew, J. Strongly constrained and appropriately normed semilocal density functional. *Phys. Rev. Lett.* **115**, 1–6 (2015).
42. Sun, J. et al. Accurate first-principles structures and energies of diversely bonded systems from an efficient density functional. *Nat. Chem.* **8**, 831–836 (2016).
43. Chakraborty, A., Dixit, M., Aurbach, D. & Major, D. T. Predicting accurate cathode properties of layered oxide materials using the SCAN meta-GGA density functional. *npj Comput. Mater.* **4**, 46–49 (2018).
44. Buda, I. G. et al. Characterization of thin film materials using SCAN meta-GGA, an accurate nonempirical density functional. *Sci. Rep.* **7**, 1–8 (2017).
45. Ewald, P. P. Die Berechnung optischer und elektrostatischer Gitterpotentiale. *Annalen der Physik* **369**, 253–287 (1921).
46. Xiao, R., Li, H. & Chen, L. Density functional investigation on Li_2MnO_3 . *Chem. Mater.* **24**, 4242–4251 (2012).
47. Wang, S., Liu, J. & Sun, Q. New allotropes of Li_2MnO_3 as cathode materials with better cycling performance predicted in high pressure synthesis. *J. Mater. Chem. A* **5**, 16936–16943 (2017).
48. Gu, M. et al. Formation of the spinel phase in the layered composite cathode used in Li-ion batteries. *ACS Nano* **7**, 760–767 (2013).
49. Baur, C. et al. Improved cycling stability in high-capacity Li-rich vanadium containing disordered rock salt oxyfluoride. *J. Mater. Chem. A* **2**, 21244–21253 (2019).
50. Raebiger, H., Lany, S. & Zunger, A. Charge self-regulation upon changing the oxidation state of transition metals in insulators. *Nature* **453**, 763–766 (2008).
51. Radin, M. D., Vinckeviciute, J., Seshadri, R. & Van der Ven, A. Manganese oxidation as the origin of the anomalous capacity of Mn-containing Li-excess cathode materials. *Nat. Energy* **4**, 639–646 (2019).
52. Davis, R.; Whitten, K. W. *General Chemistry* (Saunders golden sunburst series; Saunders College Publishing, 1996).
53. Britto, S. et al. Multiple redox modes in the reversible lithiation of high-capacity, peierls-distorted vanadium sulfide. *J. Am. Chem. Soc.* **137**, 8499–8508 (2015).
54. Christensen, R., Hansen, H. A., Dickens, C. F., Nørskov, J. K. & Vegge, T. Functional independent scaling relation for ORR/OER catalysts. *J. Phys. Chem. C* **120**, 24910–24916 (2016).
55. Loftager, S., Schougaard, S., Vegge, T. & García Lastra, J. Density functional theory study of redox potential shifts in $\text{Li}_x\text{Mn}_y\text{Fe}_{1-y}\text{PO}_4$ battery electrodes. *J. Phys. Chem. Part C* **123**, 102–109 (2019).
56. Lee, E. & Persson, K. A. Structural and chemical evolution of the layered Li-excess Li_2MnO_3 as a function of Li content from first-principles calculations. *Adv. Energy Mater.* **4**, 1400498 (2014).
57. Gent, W. E. et al. Coupling between oxygen redox and cation migration explains unusual electrochemistry in lithium-rich layered oxides. *Nat. Commun.* **8**, 2091 (2017).
58. Croy, J. R. et al. First-charge instabilities of layered-layered lithium-ion-battery materials. *Phys. Chem. Phys.* **17**, 24382–24391 (2015).
59. Kim, S. et al. Material design of high-capacity Li-rich layered-oxide electrodes: Li_2MnO_3 and beyond. *Energy Environ. Sci.* **10**, 2201–2211 (2017).
60. Ben Yahia, M., Vergnet, J., Saubanière, M. & Doublet, M. L. Unified picture of anionic redox in Li/Na-ion batteries. *Nat. Mater.* **18**, 496–502 (2019).
61. Stomberg, R., Jagner, S., Husebye, S., Hinsche, G. & Uhlemann, E. The crystal structure of potassium fluorooxidoperoxovanadate(V), $\text{K}_2[\text{VFO}(\text{O}_2)_2]$. *Acta Chem. Scand.* **38a**, 223–228 (1984).
62. Toukmaji, A. Y. & Board, J. A. Ewald summation techniques in perspective: a survey. *Comput. Phys. Commun.* **95**, 73–92 (1996).
63. Fennell, C. J. & Gezelter, J. D. Is the Ewald summation still necessary? Pairwise alternatives to the accepted standard for long-range electrostatics. *J. Chem. Phys.* **124**, 234104 (2006).
64. Ong, S. P. et al. Python materials genomics (pymatgen): a robust, open-source python library for materials analysis. *Comput. Mater. Sci.* **68**, 314–319 (2013).
65. Larsen, A. et al. The atomic simulation environment—a python library for working with atoms. *J. Phys. Condens. Matter* **29**, 273002 (2017).
66. Chang, J. H. et al. CLEASE: a versatile and user-friendly implementation of cluster expansion method. *J. Phys. Condens. Matter* **31**, 325901 (2019).
67. Kresse, G. & Furthmüller, J. Efficient iterative schemes for ab initio total-energy calculations using a plane-wave basis set. *Phys. Rev. B* **54**, 11169–11186 (1996).
68. Kresse, G. & Furthmüller, J. Efficiency of ab-initio total energy calculations for metals and semiconductors using a plane-wave basis set. *Comput. Mater. Sci.* **6**, 15–50 (1996).
69. Blöchl, P. E. Projector augmented-wave method. *Phys. Rev. B* **50**, 17953–17979 (1994).
70. Monkhorst, H. J. & Pack, J. D. Special points for Brillouin-zone integrations. *Phys. Rev. B* **13**, 5188–5192 (1976).
71. Dudarev, S. L., Botton, G. A., Savrasov, S. Y., Humphreys, C. J. & Sutton, A. P. Electron-energy-loss spectra and the structural stability of nickel oxide: an LSDA +U study. *Phys. Rev. B* **57**, 1505 (1998).

ACKNOWLEDGEMENTS

A.S.T. and J.M.G.L. acknowledge support from the Villum Foundation's Young Investigator Programme (4th round, project: In silico design of efficient materials for next generation batteries. Grant number: 10096). We acknowledge support from the European Union's Horizon 2020 research and innovation programme under grant agreement No 711792 (FET-OPEN project LiRichFCC).

AUTHOR CONTRIBUTIONS

A.S.T. performed all the calculations and wrote all the scripts for the analysis of the data. A.S.T., J.H.C., and J.M.G.L. designed the project and analyzed the results. All the authors contributed to the writing and revising of the manuscript.

COMPETING INTERESTS

The authors declare no competing interests.

ADDITIONAL INFORMATION

Supplementary information is available for this paper at <https://doi.org/10.1038/s41524-020-0335-4>.

Correspondence and requests for materials should be addressed to J.H.C. or J.M.G.-L.

Reprints and permission information is available at <http://www.nature.com/reprints>

Publisher's note Springer Nature remains neutral with regard to jurisdictional claims in published maps and institutional affiliations.



Open Access This article is licensed under a Creative Commons Attribution 4.0 International License, which permits use, sharing, adaptation, distribution and reproduction in any medium or format, as long as you give appropriate credit to the original author(s) and the source, provide a link to the Creative Commons license, and indicate if changes were made. The images or other third party material in this article are included in the article's Creative Commons license, unless indicated otherwise in a credit line to the material. If material is not included in the article's Creative Commons license and your intended use is not permitted by statutory regulation or exceeds the permitted use, you will need to obtain permission directly from the copyright holder. To view a copy of this license, visit <http://creativecommons.org/licenses/by/4.0/>.

© The Author(s) 2020